Three-Variable Reduction of the Spin-Flip Model for Spin-VCSELs

Mike Adams⃝, Nianqiang Li⃝, Yu Huang⃝, Pei Zhou⃝, *Member, IEEE*, and Ian Henning⃝

Abstract—Recent increased interest in spin-polarised vertical-cavity surface-emitting lasers (spin-VCSELs) as potential high-speed sources has spurred research into the analysis of their dynamics. This has often been explored by combining the spin-flip model (SFM) with numerical methods. However, numerical simulation does not readily expose key dependencies and to date there is a lack of accessible closed-form analytical results for the steady-state solutions and dynamic stability boundaries. Thus in the present contribution we address this and show that, for zero dichroism, the five rate equations of the SFM can be reduced to a set of three. These can be solved in the steady-state in terms of the intensity and polarisation of the pump (optical or electrical), and the ellipticity of the output. Additionally, a small-signal analysis leads to analytic results for the boundaries between stable and unstable operation in the plane of pump ellipticity versus pump intensity. Comparison of the results from these expressions with those from numerical bifurcation and continuation methods shows very good agreement. The accuracy of the reduced set of equations is confirmed by comparing the results with those from the full set of SFM equations. In the limiting case of very high birefringence, as would be required for a potential THz source, a simple algebraic relation is derived for the spin relaxation rate in terms of other parameters. Hence we find that the range of spin relaxation rates to achieve THz oscillations is very limited. The relative simplicity of the present approach thus offers a rapid, intuitive and convenient route to study the dynamics of spin-VCSELs.

Index Terms—Spin-VCSELs, laser arrays, laser dynamics, terahertz source, spin flip model, coupled lasers.

I. INTRODUCTION

SPIN-VCSELS allow the control of output polarisation by injection of spin-polarised carriers (for a recent review with copious references to the literature, see [1]). Amongst the proposed advantages of these devices over conventional lasers, the promise of very high speed operation [2] has recently excited much attention. It has been shown that high material birefringence can lead to frequency splitting [3] that enables ultra-fast polarisation modulation [4], [5] and a possible route to a practical terahertz source [6]. The birefringence can be increased by applying strain [3]–[5], heating [7] or the incorporation of an integrated surface grating [8]. These approaches have demonstrated maximum birefringence splittings of 259 GHz, 60 GHz and 98 GHz, respectively.

The spin-flip model (SFM) is well-established as a theoretical description of polarisation effects in VCSELs [9], [10], and has also been modified to include the polarisation of the pump [11] as is the case in spin-VCSELs. The SFM is conventionally expressed in terms of 6 coupled rate equations: 2 for the left- and right-circularly polarised (LCP, RCP) field amplitudes, 2 for the corresponding phases, and 2 for spin-up and spin-down carrier concentrations. Since only the phase difference between the fields is significant, the number of equations can be reduced to 5. The fundamental parameters involved in these equations are the carrier recombination rate γ, photon field decay rate κ, spin relaxation rate γ_s, linewidth enhancement factor α, birefringence rate γ_p and dichroism rate, γ_a. The SFM equations can also be recast in terms of light intensities, using either circularly-polarised [12], [13] or linearly-polarised [14] components, in each case allowing some simplification of approaches to finding solutions under certain assumptions. The basic SFM has also been developed in order to include, amongst other details, misalignment between the principal axes of the birefringence and dichroism [15], spectral models for the gain and the index of refraction [16], spatial variation of the electromagnetic modes and the carrier densities [17], and inclusion of thermal effects [18].

It has already been mentioned that the SFM parameters include the rates of birefringence and dichroism, and that the former is key to achieving ultra-high speed performance. In reality, however, this is an approximation since these anisotropies originate from interfacial, surface and strain

effects within the VCSEL structure [19]. Hence a more accurate model to account for these non-local anisotropies is based on a matrix approach which yields the spatial distribution of the electromagnetic modes of the spin-VCSEL [6], [20]. This model is particularly well suited also to model the effects of an integrated surface grating in order to tailor the high-speed performance of the device [6]. Another model that takes account of spatial effects has been developed to describe the dynamics of arrays of coupled spin-VCSELs [21], [22].

The SFM combined with the largest Lyapunov exponent (LLE) technique has been applied to find the regions of stable and unstable behaviour in maps of the pump polarisation P versus the total pump intensity η for various sets of device parameters [23], [24]. Negative values of the LLE correspond to stability, zero to oscillatory behaviour, and positive values to regions of more complex dynamics tending toward chaos as the LLE increases. The frequency of the polarisation oscillations is determined by the birefringence, as already discussed above. Polarisation switching and stability boundaries in spin-VCSELs have also been studied with the SFM using combinations of asymptotic and numerical methods [25], [26]. Period-doubling or quasiperiodic routes to chaos were found as either the pump magnitude or polarization ellipticity was varied. These studies resulted in a better understanding of the high-frequency oscillations [27] as well as a proposal for a secure communications system based on a master-slave configuration of two spin-VCSELs [28]. A 1310 nm dilute nitride spin-VCSEL subject to optical injection has been used to demonstrate experimentally the control of emitted light polarisation [29] as well as circular polarisation switching and polarisation bistability [30]. The SFM equations, suitably modified to include polarised optical injection [31] have shown very good agreement with experiment [29]. Recently the SFM equations have been modified to describe the nonlinear dynamics of spin-VCSELs subject to optical feedback from a mirror [32]. Maps were presented in the plane of feedback strength versus feedback delay time as well as in the P-η plane, and a powerful 0-1 test was used to determine regions of chaos. Furthermore, a comprehensive SFM-based numerical analysis of high-frequency polarisation oscillations and modulation in optically-pumped spin-VCSELs has given a deeper understanding of the influence of birefringence and spin relaxation rates [33].

It should be clear from the discussion above that, although more complex models are now becoming available to aid the design and analysis of spin-VCSELs for specific applications, the more basic and intuitive SFM approach is still extremely useful and versatile for exploring their dynamics. Since there are no analytical solutions of the time-dependent SFM equations numerical methods are usually employed, thus making it difficult to see trends with parameter values, especially since there are 6 material parameters (γ, κ, γ_s, α, γ_p, γ_a) as well as 2 operating parameters (P, η) for even the simplest solitary VCSEL. In order to simplify the problem, taking account of the fast time-scale of the spin relaxation, adiabatic elimination of the difference between the spin carrier concentrations is sometimes used. This can yield rate equations in two [34]–[37] and three [38]–[40] variables. However, it has recently been

pointed out that these do not account for some dynamic effects of the system, including polarisation chaos [41]. Furthermore, whilst the improved three-variable reduction obtained via the method of multiple scales has been very successful in accounting for experimental results on polarisation switching in conventional VCSELs (see, e.g., [42], [43]), its extension to reveal the key importance of the spin carrier population difference in spin-VCSELs has not been reported. In the present contribution a three-variable reduction of the SFM equations specifically for spin-VCSELs is presented and used to derive steady-state solutions and stability boundaries for dynamic states.

II. Theory

The SFM equations can be expressed in terms of the RCP and LCP field amplitudes, R_+, R_-, and phase difference φ by using the amplitude/phase decomposition of the fields $E_\pm = R_\pm \exp(\mathrm{i}\psi_\pm)$ and defining $\varphi = \psi_+ - \psi_-$. Allowing for polarised pumping with ellipticity P and setting the dichroism rate γ_a to zero, the equations become

$$\frac{dR_+}{dt} = \kappa \left(N + m - 1 \right) R_+ - \gamma_p R_- \sin \phi \tag{1}$$

$$\frac{dR_-}{dt} = \kappa \left(N - m - 1 \right) R_- + \gamma_p R_+ \sin \phi \tag{2}$$

$$\frac{d\phi}{dt} = 2\kappa \alpha m + \gamma_p \left(\frac{R_+}{R_-} - \frac{R_-}{R_+} \right) \cos \phi \tag{3}$$

$$\frac{dN}{dt} = \gamma \left[\eta - \left(1 + R_+^2 + R_-^2 \right) N - \left(R_+^2 - R_-^2 \right) m \right] \tag{4}$$

$$\frac{dm}{dt} = \gamma P \eta - \left[\gamma_s + \gamma \left(R_+^2 + R_-^2 \right) \right] m - \gamma \left(R_+^2 - R_-^2 \right) N \tag{5}$$

The normalised carrier variables N and m here are defined as $(n^+ + n)/2$ and $(n^+ - n)/2$, respectively, where n^+, n are the normalised spin-up/down carrier concentrations. The normalised pumping rate, denoted by η, is the sum of the RCP and LCP normalised pumping rates, and the other parameters have been defined above

Following previous work [36], [37], it is assumed that $\gamma \ll \kappa$, and that equation (4) can be replaced by an energy conservation relation:

$$R_+^2 + R_-^2 = \eta - 1. \tag{6}$$

It is then possible to reduce the remaining equations (1)-(3) and (5) to the three equations:

$$\frac{d\psi}{dt} = -2\kappa m \cos \psi + 2\gamma_p \sin \phi \tag{7}$$

$$\frac{d\phi}{dt} = 2\kappa \alpha m - 2\gamma_p \cos \phi \tan \psi \tag{8}$$

$$\frac{dm}{dt} = \gamma P \eta - \left[\gamma_s + \gamma \left(\eta - 1 \right) \cos^2 \psi \right] m + \gamma \left(\eta - 1 \right) \sin \psi \tag{9}$$

where the variable ψ is defined by $R_-/R_+ = \tan \left(\psi/2 + \pi/4 \right)$. The derivation of (7)-(9) follows the method given in [44] for the case of coupled mode rate equations, and is outlined in Appendix A.

The steady-state solutions of (7)-(9) can be expressed in terms of the ellipticity ε of the output, given by

$$\varepsilon = \frac{R_+^2 - R_-^2}{R_+^2 + R_-^2} = -\sin\psi_s \tag{10}$$

where the subscript 's' denotes the steady-state value. Thus the steady-state solution for the phase φ_s is

$$\tan\phi_s = -\frac{\varepsilon}{\alpha}. \tag{11}$$

It follows that there are two sets of solutions, denoted in-phase and out-of-phase, given by

In-phase:

$$\sin\phi_s = -\frac{\varepsilon}{\sqrt{\alpha^2 + \varepsilon^2}}, \quad \cos\phi_s = \frac{\alpha}{\sqrt{\alpha^2 + \varepsilon^2}}$$

$$m_s = -\frac{\gamma_p \varepsilon}{\kappa\sqrt{(\alpha^2 + \varepsilon^2)(1 - \varepsilon^2)}} \tag{12}$$

$$P\eta = \varepsilon\left\{\eta - 1 - \frac{\gamma_p}{\gamma\kappa}\frac{\left[\gamma_s + \gamma(\eta - 1)(1 - \varepsilon^2)\right]}{\sqrt{(1 - \varepsilon^2)(\alpha^2 + \varepsilon^2)}}\right\}. \tag{13}$$

Out-of-phase:

$$\sin\phi_s = \frac{\varepsilon}{\sqrt{\alpha^2 + \varepsilon^2}}, \quad \cos\phi_s = -\frac{\alpha}{\sqrt{\alpha^2 + \varepsilon^2}},$$

$$m_s = \frac{\gamma_p \varepsilon}{\kappa\sqrt{(\alpha^2 + \varepsilon^2)(1 - \varepsilon^2)}} \tag{14}$$

$$P\eta = \varepsilon\left\{\eta - 1 + \frac{\gamma_p}{\gamma\kappa}\frac{\left[\gamma_s + \gamma(\eta - 1)(1 - \varepsilon^2)\right]}{\sqrt{(1 - \varepsilon^2)(\alpha^2 + \varepsilon^2)}}\right\}. \tag{15}$$

For high values of the spin rate γ_s, the second term in the square bracket in (13) and (15) can be neglected, in which

case we recover (18) of [37] for zero dichroism which has been shown to give accurate predictions of the polarisation response of spin-VCSELs.

Performing a standard small-signal stability analysis of (7)-(9) yields the expressions (16) – (19), as shown at the bottom of the page, for the stability boundaries (see Appendix B for details). Equations (16) and (18) are the saddle-node bifurcations; (17) and (19) are the Hopf bifurcations.

For the special case of linear polarisation (LP), $\varepsilon = 0$, (13) and (15) give the boundaries as

$$\textit{In-phase, saddle node}: \quad \eta - 1 = \frac{\gamma_s\gamma_p}{\gamma(\kappa\alpha - \gamma_p)} \tag{20}$$

$$\textit{Out-of-phase, Hopf}: \eta - 1 = \frac{1}{\gamma}(2\alpha\gamma_p - \gamma_s) \tag{21}$$

which are identical to (33) and (34) of [10] for the cases of x-LP and y-LP stability boundaries, respectively.

III. RESULTS

A. Comparison With Results From Numerical Techniques

In general, equations (16) - (19) can be solved for ε^2 by a root-finding algorithm and then (13) and (15) can be used to calculate the corresponding values of pump polarisation P. Although this is an indirect method of solution, it is significantly easier and faster than using conventional numerical techniques to find the stability boundaries. Here we take some examples to test the accuracy of our approximations against numerical techniques. For the first example we use a parameter set used previously [26], namely $\gamma = 1\,\text{ns}^{-1}$, $\kappa = 250\,\text{ns}^{-1}$, $\gamma_s = 30\,\text{ns}^{-1}$, $\alpha = 3$, $\gamma_p = 150\,\text{ns}^{-1}$ and $\gamma_a = 0$. Fig. 1 shows regions of stability and instability in a plot of pump polarisation P versus the total pump intensity η. Fig. 1(a) shows the results of a bifurcation analysis where numerical solution of the reduced rate equations (7) – (9) are used to find intensity extrema at each point (η, P). The number of

$$\textit{In-phase}: \quad \gamma_p\left[\gamma_s + \gamma(\eta - 1)(1 - \varepsilon^2)\right]\left[\frac{\alpha^2 + \varepsilon^4}{(\alpha^2 + \varepsilon^2)(1 - \varepsilon^2)}\right] - \gamma(\eta - 1)\left[\kappa\sqrt{(\alpha^2 + \varepsilon^2)(1 - \varepsilon^2)} + 2\gamma_p\varepsilon^2\right] > 0 \tag{16}$$

$$-\frac{8\gamma_p^2\varepsilon^2}{(\alpha^2 + \varepsilon^2)(1 - \varepsilon^2)}\left[\frac{\gamma_p(\alpha^2 + \varepsilon^4)}{\sqrt{(\alpha^2 + \varepsilon^2)(1 - \varepsilon^2)}} - \gamma_s\varepsilon^2\right] + 2\gamma\gamma_p(\eta - 1)\left[\kappa(\alpha^2 - \varepsilon^2)\sqrt{\frac{1 - \varepsilon^2}{\alpha^2 + \varepsilon^2}} + 2\gamma_p\varepsilon^2\right]$$

$$+\left[\gamma_s + \gamma(\eta - 1)(1 - \varepsilon^2)\right]\left[-2\gamma_p\gamma_s\frac{\varepsilon^2}{\sqrt{(\alpha^2 + \varepsilon^2)(1 - \varepsilon^2)}} + \kappa\gamma(\eta - 1)(1 - \varepsilon^2)\right] > 0 \tag{17}$$

$$\textit{Out-of-phase}: \quad \gamma_p\left[\gamma_s + \gamma(\eta - 1)(1 - \varepsilon^2)\right]\left[\frac{\alpha^2 + \varepsilon^4}{(\alpha^2 + \varepsilon^2)(1 - \varepsilon^2)}\right] + \gamma(\eta - 1)\left[\kappa\sqrt{(\alpha^2 + \varepsilon^2)(1 - \varepsilon^2)} - 2\gamma_p\varepsilon^2\right] > 0 \tag{18}$$

$$\frac{8\gamma_p^2\varepsilon^2}{(\alpha^2 + \varepsilon^2)(1 - \varepsilon^2)}\left[\frac{\gamma_p(\alpha^2 + \varepsilon^4)}{\sqrt{(\alpha^2 + \varepsilon^2)(1 - \varepsilon^2)}} + \gamma_s\varepsilon^2\right] - 2\gamma\gamma_p(\eta - 1)\left[\kappa(\alpha^2 - \varepsilon^2)\sqrt{\frac{1 - \varepsilon^2}{\alpha^2 + \varepsilon^2}} - 2\gamma_p\varepsilon^2\right]$$

$$+\left[\gamma_s + \gamma(\eta - 1)(1 - \varepsilon^2)\right]\left[2\gamma_p\gamma_s\frac{\varepsilon^2}{\sqrt{(\alpha^2 + \varepsilon^2)(1 - \varepsilon^2)}} + \kappa\gamma(\eta - 1)(1 - \varepsilon^2)\right] > 0 \tag{19}$$
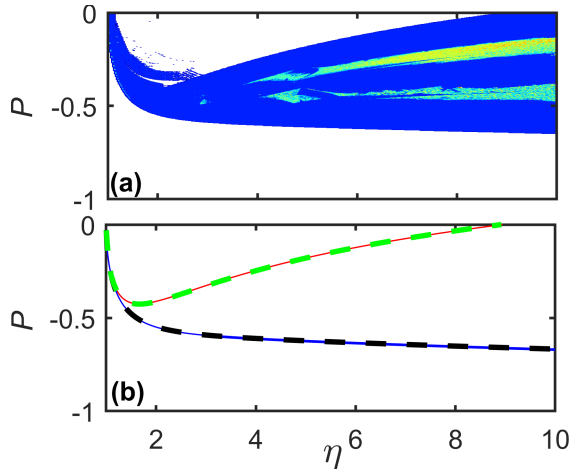
Fig. 1. Comparison of numerical results with those from equations (17), (13) and (19), (15). The parameters used are $\gamma_a = 0$, $\kappa = 250$ ns^{-1}, $\gamma = 1$ ns^{-1}, $\gamma_p = 150$ ns^{-1}, $\alpha = 3$ and $\gamma_s = 30$ ns^{-1}. (a) Numerical bifurcation analysis. (b) Solid line represents the AUTO results, the dash line represents the analytical solutions. White, blue and cyan, respectively denote regions of CW operation, P1 and P2 oscillation.

extrema corresponds to the local dynamic regime, i.e. 1 to CW operation, 2 to period one (P1) oscillation, 4 to period two (P2), denoted by white, blue and cyan, respectively. More intensity extrema correspond to complex dynamics and chaos, denoted by yellow to red. Fig. 1(b) shows a comparison between the Hopf bifurcations found using the continuation package AUTO [45] and those calculated from (17) with (13), and (19) with (15). The agreement of the latter is very good over the whole range plotted.

For our second example (Fig. 2) we consider again the parameters $\gamma = 1$ ns^{-1}, $\kappa = 250$ ns^{-1}, $\alpha = 3$ and $\gamma_a = 0$, but now with a range of values each of γ_s and γ_p. In this case the left panel shows the bifurcation diagrams for the full set of equations (1) – (5) and the right panel shows those for the reduced set (7) – (9). There is generally encouraging agreement between the two sets of results with some small differences in the detail of the dynamics. The centre panel shows the comparison between AUTO results for the Hopf bifurcations and those from (17) with (13), and (19) with (15). Again the agreement is very satisfactory. The unusual feature revealed by AUTO in plots (d3) and (d4) (upper right corner of each) of the centre panel of Fig 2 is thought to be due to another bifurcation: the saddle-node of limit cycles (LPC) as seen, for example, in Fig. 11(c) of [26] and Fig. 3(b3),(b4) of [33]. In summary, the results of Fig 2 validate (1) the three-variable reduction of the SFM equations and (2) the algebraic expressions derived for the bifurcations based on this reduction.

B. Low Values of Birefringence

Here we focus on the situation of low values of birefringence and high spin rate. In this case one of the Hopf bifurcations disappears and the limit of stability is instead formed by the saddle-node (SN) bifurcation. Fig. 3 shows results for the same parameters as Fig. 2 but now with $\gamma_s = 90$ ns^{-1} and $\gamma_p = 5\pi$ ns^{-1}, 4.5π ns^{-1} and 2π ns^{-1}. Here the disappearance of the out-of-phase Hopf bifurcation

occurs for $\gamma_p < 4.775\pi$ ns^{-1}. So now we compare results from AUTO with those from (16) and (17) with (13). Here there is excellent agreement between the results AUTO for the SN bifurcations with those of (16) with (13). For the Hopf bifurcations, although the general trends are similar for the two sets of results, there are again unusual features due to other bifurcations that are revealed by AUTO which are not present in the analytic results.

C. Limiting Case of High Birefringence

For potential applications as a source of THz radiation [6] it is relevant to study the case of very high birefringence rate γ_p, since the corresponding oscillation frequency is dominated by the term γ_p/π [2], [11]. In the limit of high γ_p, we find that the absolute values of output ellipticity ε are very much less than 1 and it is possible to obtain quite accurate results from series expansions of the expressions for the stability boundaries to order ε^2. Performing these expansions on (17) and (19) yields the following expression for the Hopf boundaries:

$$\varepsilon \cong \pm \frac{\alpha}{2\gamma_p}\sqrt{\kappa\gamma(\eta - 1)} \tag{22}$$

The corresponding expression for the relationship between the pump ellipticity and pump intensity is

$$P \cong \pm \frac{\sqrt{\eta - 1}}{2\eta}\left\{\frac{\alpha}{\gamma_p}(\eta - 1)\sqrt{\kappa\gamma} \mp \frac{[\gamma_s + \gamma(\eta - 1)]}{\sqrt{\kappa\gamma}}\right\} \tag{23}$$

where the first $+/-$ is for the sign of the output ellipticity and the second is for in-phase or out-of-phase solutions. The latter result shows that there are very small regions of instability for very high values of γ_p, one very near threshold and the other at high pump intensity for pump polarisations very close to circular.

This is consistent with numerical results of stability maps presented in our companion paper [33] where birefringence rates up to 300 ns^{-1} were considered. For the present case of higher values of birefringence, (23) implies a narrow range of spin relaxation rates where polarisation oscillations are predicted under these conditions. To illustrate this, we re-write (23) for the case $P = -1$ in the form

$$[\gamma_s + \gamma(\eta - 1)] \cong 2\eta\sqrt{\frac{\kappa\gamma}{\eta - 1}} \pm \frac{\alpha\kappa\gamma}{\gamma_p}(\eta - 1). \tag{24}$$

This result is plotted in the $\gamma_p/\pi - \gamma_s$ plane in Fig. 4 for values of $\gamma = 1$ ns^{-1}, $\kappa = 225$ ns^{-1}, $a = 3$ and $\eta = 2$, 5 and 10. The range of polarisation oscillation frequencies is from 200 to 500 GHz, thus extending the range considered in [33] into that for a potential terahertz source. Fig.4 shows that at a frequency of 200 GHz the range $\Delta\gamma_s$ of spin rate for oscillation is 2.1 ns^{-1} 8.6 ns^{-1} and 19.3 ns^{-1} for $\eta = 2$, 5 and 10, respectively. At the frequency of 500 GHz these values reduce to 0.9 ns^{-1} 3.4 ns^{-1} and 7.6 ns^{-1}, respectively.

It follows from (24) that in the limiting case of high birefringence, $\gamma_p \rightarrow \infty$, the spin rate $\gamma_{s\infty}$ required is
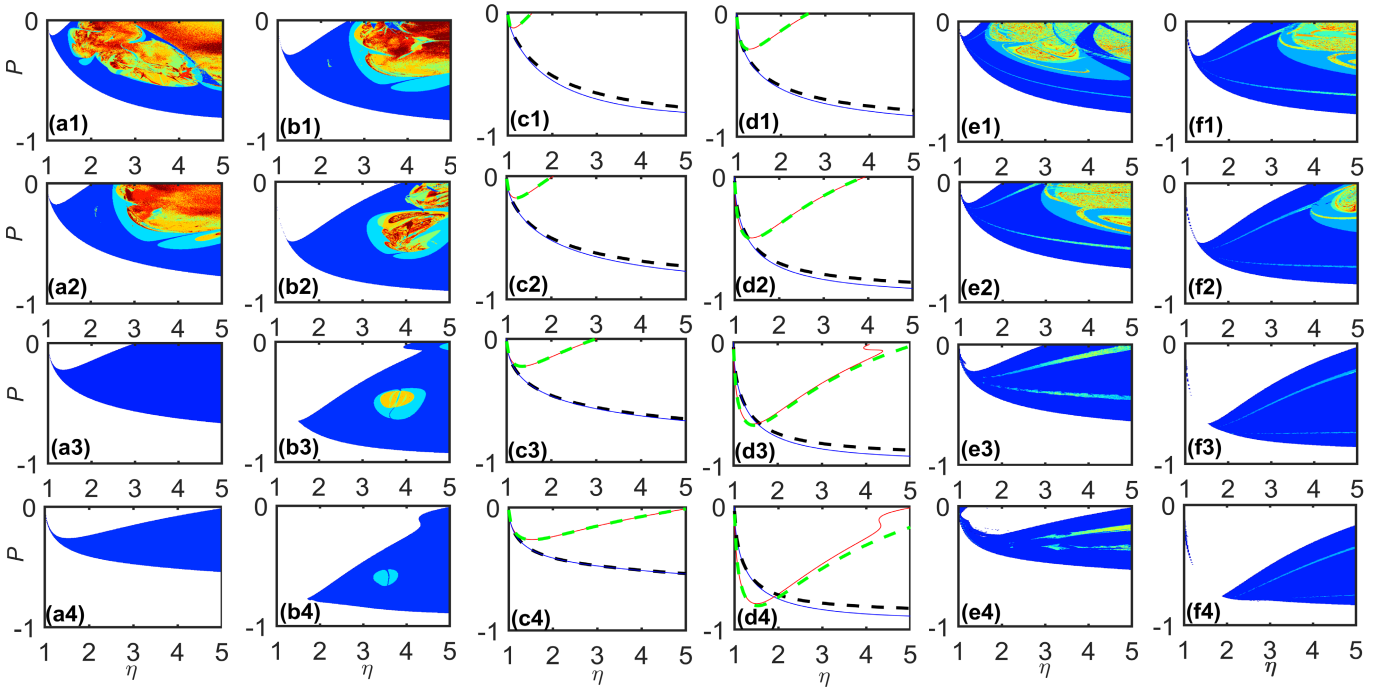
Fig. 2. Comparison of numerical results with those from equations (17), (13) and (19), (15). Left and right: bifurcation diagrams in the (η, P) plane calculated from $|E^+|^2$. (a1, c1, e1) $\gamma_p = 5\pi$ ns^{-1}, (a2, c2, e2) $\gamma_p = 10\pi$ ns^{-1}, (a3, c3, e3) $\gamma_p = 20\pi$ ns^{-1}, and (a4, c4, e4) $\gamma_p = 40\pi$ ns^{-1}, where $\gamma_s = 20$ ns^{-1}. (b1, d1, f1) $\gamma_s = 30$ ns^{-1}, (b2, d2, f2) $\gamma_s = 50$ ns^{-1}, (b3, d3, f3) $\gamma_s = 70$ ns^{-1} and (b4, d4, f4) $\gamma_s = 90$ ns^{-1}, where $\gamma_p = 10\pi$ ns^{-1}. The parameters used are $\gamma_a = 0$, $\kappa = 250$ ns^{-1}, $\gamma = 1$ ns^{-1} and $\alpha = 3$. Centre: the solid line represents the AUTO results; the dash line represents the analytical solutions. White, blue and cyan, respectively, denote regions of CW operation, P1 and P2 oscillation, while more complicated dynamics including chaos is shown as yellow to red.
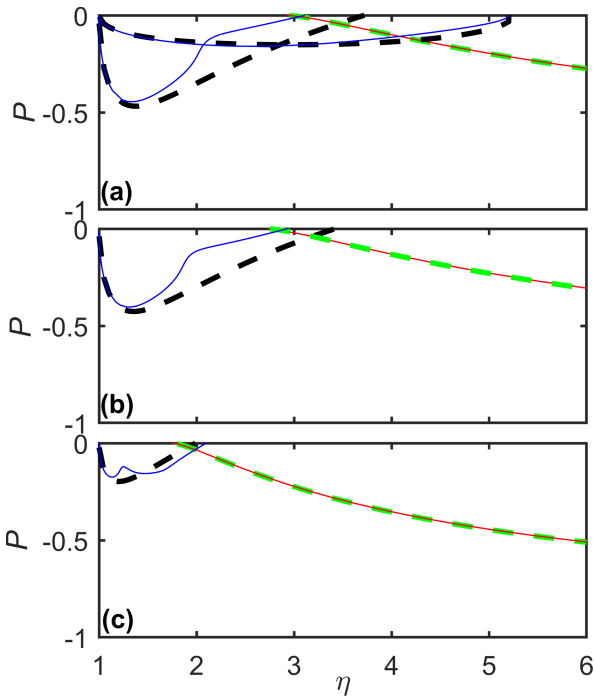

Fig. 3. Comparison of numerical results with those from equations (16) and (17) with (13), where (a) $\gamma_p = 5\pi$ ns^{-1}, (b) $\gamma_p = 4.5\pi$ ns^{-1} and (c) $\gamma_p = 2\pi$ ns^{-1}. The parameters used are $\gamma_a = 0$, $\kappa = 250$ ns^{-1}, $\gamma = 1$ ns^{-1} and $\alpha = 3$. The solid line represents the AUTO results; the dashed line represents the analytical solutions. (Hopf in blue, SN in red).

given by

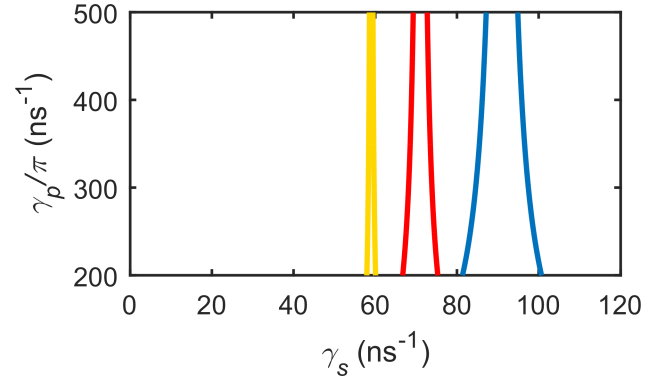$$\gamma_{s\infty} \cong 2\eta \sqrt{\frac{\kappa \gamma}{\eta - 1}} - \gamma (\eta - 1). \tag{25}$$

Fig. 4. Regions of P1 oscillations predicted by (24) for values of $\gamma = 1$ ns^{-1}, $\kappa = 225$ ns^{-1}, $a = 3$ and $\eta = 2$ (left), 5 (centre) and 10 (right).

For example, at normalised pump intensities of 2, 5 and 10 the values of $\gamma_{s\infty}$ are 59 ns^{-1} 71 ns^{-1} and 91 ns^{-1}, respectively, for the parameters used in Fig. 4. The corresponding variation $\Delta \gamma_s$ of spin rate to give oscillation at frequency γ_p / π is given by

$$\Delta \gamma_s \cong \frac{2\alpha \kappa \gamma}{\gamma_p} (\eta - 1). \tag{26}$$

Hence for oscillation of frequency 1 THz at normalised pump intensities of 2, 5 and 10, the values of $\Delta \gamma_s$ are 0.4 ns^{-1} 1.7 ns^{-1} and 3.9 ns^{-1}, respectively, for the parameters used in Fig. 4.

Achieving such tight tolerances in practice would be very challenging and this increases the difficulty of generating THz oscillations by this means.

IV. CONCLUSION

In this paper we report on how the five coupled rate equations of the SFM with zero dichroism can be reduced to a system of three equations. The variables in these equations are the phase difference between the LCP and RCP fields, the ratio of the LCP and RCP field amplitudes (expressed as an angle) and the difference between the normalised spin-up and spin-down carrier densities. The underlying physical parameters are the carrier recombination rate γ, photon field decay rate κ, spin relaxation rate γ_s, linewidth enhancement factor α, birefringence rate γ_p, pump polarisation P and total pump intensity η. Whilst closed-form steady-state solutions for P as a function of η are not possible, indirect solutions for the ellipticity ε of the output in terms of η and for P in terms of ε and η are found. For the special case of linear polarisation these expressions reduce to those derived previously by other authors. In the general case of elliptical polarisation there are two sets of solutions, corresponding to in-phase and out-of-phase operation where this notation indicates the quadrant in which the phase difference between the LCP and RCP fields lies.

A small-signal analysis of the reduced equations has revealed closed-form expressions that predict the boundaries of stable operation. Comparison of results from these expressions with those found from conventional numerical bifurcation and continuation methods for a range of parameter sets has shown a very satisfactory level of agreement. This agreement is confirmed also by comparison of bifurcation diagrams in the P-η plane found from the full set and the reduced set of equations. In the limit of very high birefringence, simple approximations are derived which show that the ranges of instability are very small and restricted to pump polarisations close to circular with spin rates that need to be controlled to a high degree of precision. This result reveals key requirements to exploit ultra-high frequency polarisation oscillations as the basis for a source of terahertz radiation with spin-VCSELs. The relative simplicity and convenience of the analytic results for steady-state solutions and stability conditions offer enhanced physical insight and reveal trends with parameters that are much more time-consuming to achieve if attempted by conventional numerical methods.

APPENDIX A
DERIVATION OF EQUATIONS (7) – (9)

Using the conservation law (6), we define a new variable ψ :

$$R_+ = \sqrt{\eta - 1} \cos\left(\frac{\psi + \pi/2}{2}\right),$$
$$R_- = \sqrt{\eta - 1} \sin\left(\frac{\psi + \pi/2}{2}\right). \tag{A1}$$

From (6) it follows that

$$\frac{d\left(R_+^2 + R_-^2\right)}{dt} = 0. \tag{A2}$$

Hence, from (1) and (2),

$$\frac{d\left(R_+^2 + R_-^2\right)}{dt} = 2\kappa\,(N-1)\left(R_+^2 + R_-^2\right)$$
$$+ 2\kappa m\left(R_+^2 - R_-^2\right) = 0. \tag{A3}$$

Using (A1), (A3) becomes

$$N - 1 = m\sin\psi. \tag{A4}$$

From the definitions (A1), we have

$$\frac{dR_+}{dt} = -\frac{R_+}{2}\tan\left(\frac{\psi + \pi/2}{2}\right)\frac{d\psi}{dt},$$
$$\frac{dR_-}{dt} = \frac{R_-}{2}\cot\left(\frac{\psi + \pi/2}{2}\right)\frac{d\psi}{dt}. \tag{A5}$$

Hence equations (1) and (2) can be transformed to

$$\frac{d\psi}{dt} = -2\kappa\,(N+m-1)\cot\left(\frac{\psi + \pi/2}{2}\right) + 2\gamma_p\sin\phi, \tag{A6}$$

$$\frac{d\psi}{dt} = 2\kappa\,(N-m-1)\tan\left(\frac{\psi + \pi/2}{2}\right) + 2\gamma_p\sin\phi. \tag{A7}$$

Multiplying (A6) by $\tan[(\psi + \pi/2)/2]$ and (A7) by $\cot[(\psi + \pi/2)/2]$, and adding gives (7). Using (A1) in (3) gives (8).

Similarly, (5) becomes

$$\frac{dm}{dt} = \gamma\,P\eta - \left[\gamma_s + \gamma\,(\eta-1)\right]m + \gamma\,(\eta-1)\,N\sin\psi \tag{A8}$$

Substituting for N from (A4), gives (9).

APPENDIX B
SMALL-SIGNAL STABILITY ANALYSIS OF THE REDUCED EQUATIONS

The perturbed solutions of (7) - (9) are $m = m_s + \Delta m\,e^{\lambda t}$, $\varphi = \varphi_s + \Delta\varphi e^{\lambda t}$ and $\psi = \psi_s + \Delta\psi e^{\lambda t}$ where $\Delta m \ll m_s$, $\Delta\varphi \ll \varphi_s$ and $\Delta\psi \ll \psi_s$. It follows that, to first order in small quantities, the resulting equations can be combined into a cubic equation of the form

$$\lambda^3 + A_1\lambda^2 + A_2\lambda + A_3 = 0 \tag{B1}$$

where the coefficients A_i are given by

$$A_1 = \gamma_s + \gamma\,(\eta-1)\cos^2\psi_s - 4\gamma_p\sin\phi_s\tan\psi_s, \tag{B2}$$

$$A_2 = 4\gamma_p^2\left[(\sin\phi_s\tan\psi_s)^2 + \left(\frac{\cos\phi_s}{\cos\psi_s}\right)^2\right]$$
$$- 4\gamma_p\gamma_s\sin\phi_s\tan\psi_s + 2\kappa\gamma\,(\eta-1)\cos^2\psi_s, \tag{B3}$$

$$A_3 = 4\gamma_p^2\left[\gamma_s + \gamma\,(\eta-1)\cos^2\psi_s\right]$$
$$\times\left[(\sin\phi_s\tan\psi_s)^2 + \left(\frac{\cos\phi_s}{\cos\psi_s}\right)^2\right]$$
$$- 4\gamma\,\gamma_p\,(\eta-1)\cos\psi_s\,(\kappa + 2\gamma_p\sin\phi_s\tan\psi_s)$$
$$\times(\alpha\cos\phi_s + \sin\phi_s\sin\psi_s). \tag{B4}$$

The conditions for stable steady-state solutions of (B1) are

$$A_1 > 0, \quad A_3 > 0, \quad A_1A_2 - A_3 > 0 \tag{B5}$$

The second condition of (B5) is

$$
\gamma_p \left[\gamma_s + \gamma \left(\eta - 1 \right) \cos^2 \psi_s \right] \left[\left(\sin \phi_s \tan \psi_s \right)^2 + \left(\frac{\cos \phi_s}{\cos \psi_s} \right)^2 \right]
$$
$$
- \gamma \left(\eta - 1 \right) \cos \psi_s \left(\kappa + 2 \gamma_p \sin \phi_s \tan \psi_s \right)
$$
$$
\times \left(\alpha \cos \phi_s + \sin \phi_s \sin \psi_s \right) > 0. \tag{B6}
$$

Substituting the in-phase and out-of-phase steady-state solutions from (12) and (14) yields (16) and (18), respectively.

The third condition of (B5) is

$$
-16 \gamma_p^2 \sin \phi_s \tan \psi_s \left[\gamma_p \left(\sin \phi_s \tan \psi_s \right)^2 + \gamma_p \left(\frac{\cos \phi_s}{\cos \psi_s} \right)^2 \right.
$$
$$
\left. - \gamma_s \sin \phi_s \tan \psi \right] + \left[\gamma_s + \gamma \left(\eta - 1 \right) \cos^2 \psi_s \right]
$$
$$
\times \left[-4 \gamma_p \gamma_s \sin \phi_s \tan \psi_s + 2 \kappa \gamma \left(\eta - 1 \right) \cos^2 \psi_s \right]
$$
$$
+ 4 \gamma \gamma_p \kappa \left(\eta - 1 \right) \cos \psi_s \left(\alpha \cos \phi_s - \sin \phi_s \sin \psi_s \right)
$$
$$
+ 8 \gamma \gamma_p^2 \left(\eta - 1 \right) \sin \phi_s \sin \psi_s \left(\alpha \cos \phi_s + \sin \phi_s \sin \psi_s \right) > 0. \tag{B7}
$$

Substituting the in-phase and out-of-phase steady-state solutions from (12) and (14) yields (17) and (19), respectively.

References

[1] I. Žutić *et al.*, "Spin-lasers: Spintronics beyond magnetoresistance," *Solid State Commun.*, vols. 316–317, Aug. 2020, Art. no. 113949.

[2] M. Lindemann *et al.*, "Ultrafast spin-lasers," *Nature*, vol. 568, no. 7751, pp. 212–215, Apr. 2019.

[3] T. Pusch, M. Lindemann, N. C. Gerhardt, M. R. Hofmann, and R. Michalzik, "Vertical-cavity surface-emitting lasers with birefringence splitting above 250 GHz," *Electron. Lett.*, vol. 51, no. 20, pp. 1600–1602, Oct. 2015.

[4] P. E. Faria, Jr., G. Xu, J. Lee, N. C. Gerhardt, G. M. Sipahi, and I. Zutic, "Towards high-frequency operation of spin-lasers," *Phys. Rev. B, Condens. Matter*, vol. 92, no. 7, Aug. 2015, Art. no. 075311.

[5] N. Yokota, K. Nisaka, H. Yasaka, and K. Ikeda, "Spin polarization modulation for high-speed vertical-cavity surface-emitting lasers," *Appl. Phys. Lett.*, vol. 113, no. 17, Oct. 2018, Art. no. 171102.

[6] M. Drong *et al.*, "Spin-VCSELs with local optical anisotropies: Toward terahertz polarization modulation," *Phys. Rev. A, Gen. Phys.*, vol. 15, no. 1, Jan. 2021, Art. no. 014041.

[7] T. Pusch, E. L. Tona, M. Lindemann, N. C. Gerhardt, M. R. Hofmann, and R. Michalzik, "Monolithic vertical-cavity surface-emitting laser with thermally tunable birefringence," *Appl. Phys. Lett.*, vol. 110, no. 15, Apr. 2017, Art. no. 151106.

[8] T. Pusch *et al.*, "Vertical-cavity surface-emitting laser with integrated surface grating for high birefringence splitting," *Electron. Lett.*, vol. 55, no. 19, pp. 1055–1057, Sep. 2019.

[9] M. S. Miguel, Q. Feng, and J. V. Moloney, "Light-polarization dynamics in surface-emitting semiconductor lasers," *Phys. Rev. A, Gen. Phys.*, vol. 52, no. 2, pp. 1728–1739, Aug. 1995.

[10] J. Martin-Regalado, F. Prati, M. S. Miguel, and N. B. Abraham, "Polarization properties of vertical-cavity surface-emitting lasers," *IEEE J. Quantum Electron.*, vol. 33, no. 5, pp. 765–783, May 1997.

[11] A. Gahl, S. Balle, and M. San Miguel, "Polarization dynamics of optically pumped VCSELs," *IEEE J. Quantum Electron.*, vol. 35, no. 3, pp. 342–351, Mar. 1999.

[12] A. Dyson and M. J. Adams, "Spin-polarized properties of optically pumped vertical cavity surface emitting lasers," *J. Opt. B, Quantum Semiclass. Opt.*, vol. 5, no. 3, pp. 222–226, Jun. 2003.

[13] M. J. Adams and D. Alexandropoulos, "Parametric analysis of spin-polarized VCSELs," *IEEE J. Quantum Electron.*, vol. 45, no. 6, pp. 744–749, Jun. 2009.

[14] G. Xu, J. D. Cao, V. Labinac, and I. Žutić, "Intensity equations for birefringent spin lasers," *Phys. Rev. B, Condens. Matter*, vol. 103, no. 4, Jan. 2021, Art. no. 045306.

[15] M. Travagnin, "Linear anisotropies and polarization properties of vertical-cavity surface-emitting semiconductor lasers," *Phys. Rev. A, Gen. Phys.*, vol. 56, no. 5, pp. 4094–4105, Nov. 1997.

[16] S. Balle, E. Tolkachova, M. S. Miguel, J. R. Tredicce, J. Martın-Regalado, and A. Gahl, "Mechanisms of polarization switching in single-transverse-mode vertical-cavity surface-emitting lasers: Thermal shift and nonlinear semiconductor dynamics," *Opt. Lett.*, vol. 24, no. 16, pp. 1121–1123, Aug. 1999.

[17] J. Mulet and S. Balle, "Spatio-temporal modeling of the optical properties of VCSELs in the presence of polarization effects," *IEEE J. Quantum Electron.*, vol. 38, no. 3, pp. 291–305, Mar. 2002.

[18] C. Masoller and M. S. Torre, "Modeling thermal effects and polarization competition in vertical-cavity surface-emitting lasers," *Opt. Exp.*, vol. 16, no. 28, pp. 21282–21296, Dec. 2008.

[19] T. Fördös, K. Postava, H. Jaffrès, and J. Pištora, "Matrix approach for modeling of emission from multilayer spin-polarized light-emitting diodes and lasers," *J. Opt.*, vol. 16, no. 6, Jun. 2014, Art. no. 065008.

[20] T. Fördös *et al.*, "Eigenmodes of spin vertical-cavity surface-emitting lasers with local linear birefringence and gain dichroism," *Phys. Rev. A, Gen. Phys.*, vol. 96, no. 4, Oct. 2017, Art. no. 043828.

[21] M. Vaughan, H. Susanto, I. Henning, and M. Adams, "The overlap factor model of spin-polarised coupled lasers," *Photonics*, vol. 8, no. 3, p. 83, Mar. 2021.

[22] M. Vaughan, H. Susanto, I. Henning, and M. Adams, "Dynamics of laterally-coupled pairs of spin-VCSELs," *IEEE J. Quantum Electron.*, vol. 56, no. 3, pp. 1–10, Jun. 2020.

[23] R. Al-Seyab, D. Alexandropoulos, I. D. Henning, and M. J. Adams, "Instabilities in spin-polarized vertical-cavity surface-emitting lasers," *IEEE Photon. J.*, vol. 3, no. 5, pp. 799–809, Oct. 2011.

[24] S. S. Alharthi, R. K. Al Seyab, I. D. Henning, and M. J. Adams, "Simulated dynamics of optically pumped dilute nitride 1300 nm spin vertical-cavity surface-emitting lasers," *IET Optoelectron.*, vol. 8, no. 2, pp. 117–121, Apr. 2014.

[25] H. Susanto, K. Schires, M. J. Adams, and I. D. Henning, "Spin-flip model of spin-polarized vertical-cavity surface-emitting lasers: Asymptotic analysis, numerics, and experiments," *Phys. Rev. A, Gen. Phys.*, vol. 92, no. 6, Dec. 2015, Art. no. 063838.

[26] N. Li, H. Susanto, B. R. Cemlyn, I. D. Henning, and M. J. Adams, "Stability and bifurcation analysis of spin-polarized vertical-cavity surface-emitting lasers," *Phys. Rev. A, Gen. Phys.*, vol. 96, no. 1, Jul. 2017, Art. no. 013840.

[27] M. S. Torre *et al.*, "High frequency continuous birefringence-induced oscillations in spin-polarized vertical-cavity surface-emitting lasers," *Opt. Lett.*, vol. 42, no. 8, pp. 1628–1631, Apr. 2017.

[28] N. Li, H. Susanto, B. Cemlyn, I. D. Henning, and M. J. Adams, "Secure communication systems based on chaos in optically pumped spin-VCSELs," *Opt. Lett.*, vol. 42, no. 17, pp. 3494–3497, Sep. 2017.

[29] S. S. Alharthi *et al.*, "Control of emitted light polarization in a 1310 nm dilute nitride spin-vertical cavity surface emitting laser subject to circularly polarized optical injection," *Appl. Phys. Lett.*, vol. 105, no. 18, Nov. 2014, Art. no. 181106.

[30] S. S. Alharthi, A. Hurtado, V.-M. Korpijarvi, M. Guina, I. D. Henning, and M. J. Adams, "Circular polarization switching and bistability in an optically injected 1300 nm spin-vertical cavity surface emitting laser," *Appl. Phys. Lett.*, vol. 106, no. 2, Jan. 2015, Art. no. 021117.

[31] R. Al-Seyab, K. Schires, A. Hurtado, I. D. Henning, and M. J. Adams, "Dynamics of VCSELs subject to optical injection of arbitrary polarization," *IEEE J. Sel. Topics Quantum Electron.*, vol. 19, no. 4, Jul. 2013, Art. no. 1700512.

[32] T. Song *et al.*, "Numerical analysis of nonlinear dynamics based on spin-VCSELs with optical feedback," *Photonics*, vol. 8, no. 1, p. 10, Jan. 2021.

[33] Y. Huang, P. Zhou, M. S. Torre, N. Li, I. D. Henning, and M. J. Adams, "Optically pumped spin-VCSELs: Toward high-frequency polarization oscillations and modulation," *IEEE J. Quantum Electron.*, vol. 57, no. 6, pp. 1–12, Dec. 2021.

[34] M. Travagnin, M. P. van Exter, and J. P. Woerdman, "Influence of carrier dynamics on the polarization stability and noise-induced polarization hopping in surface-emitting semiconductor lasers," *Phys. Rev. A, Gen. Phys.*, vol. 56, no. 2, pp. 1497–1507, Aug. 1997.

[35] M. P. van Exter, R. F. M. Hendriks, and J. P. Woerdman, "Physical insight into the polarization dynamics of semiconductor vertical-cavity lasers," *Phys. Rev. A, Gen. Phys.*, vol. 57, no. 3, pp. 2080–2090, Mar. 1998.

[36] T. Erneux, J. Danckaert, K. Panajotov, and I. Veretennicoff, "Two-variable reduction of the san Miguel–Feng–Moloney model for vertical-cavity surface-emitting lasers," *Phys. Rev. A, Gen. Phys.*, vol. 59, no. 6, pp. 4660–4667, Jun. 1999.

[37] M. Adams, N. Li, B. Cemlyn, H. Susanto, and I. Henning, "Algebraic expressions for the polarisation response of spin-VCSELs," *Semicond. Sci. Technol.*, vol. 33, no. 6, May 2018, Art. no. 064002.

[38] M. P. V. Exter, M. B. Willemsen, and J. P. Woerdman, "Effect of mode-partition noise on intensity squeezing in a two-mode laser," *J. Opt. B, Quantum Semiclass. Opt.*, vol. 1, no. 6, pp. 637–645, Dec. 1999.

[39] M. B. Willemsen, M. P. van Exter, and J. P. Woerdman, "Correlated fluctuations in the polarization modes of a vertical-cavity semiconductor laser," *Phys. Rev. A, Gen. Phys.*, vol. 60, no. 5, pp. 4105–4113, Nov. 1999.

[40] G. Van der Sande, J. Danckaert, I. Veretennicoff, and T. Erneux, "On rate equations for vertical-cavity surface-emitting lasers," *Phys. Rev. A, Gen. Phys.*, vol. 67, no. 1, Jan. 2003, Art. no. 013809.

[41] M. Virte and F. Ferranti, "Chaos-preserving reduction of the spin-flip model for VCSELs: Failure of the adiabatic elimination of the spin-population difference," *IEEE J. Sel. Topics Quantum Electron.*, vol. 25, no. 6, pp. 1–8, Nov. 2019.

[42] G. Verschaffelt *et al.*, "Frequency response of polarization switching in vertical-cavity surface-emitting lasers," *IEEE J. Quantum Electron.*, vol. 39, no. 10, pp. 1177–1186, Oct. 2003.

[43] J. Danckaert *et al.*, "Stochastic polarization switching dynamics in vertical-cavity surface-emitting lasers: Theory and experiment," *IEEE J. Sel. Topics Quantum Electron.*, vol. 10, no. 5, pp. 911–917, Sep. 2004.

[44] M. Adams, R. A. Seyab, I. Henning, H. Susanto, and M. Vaughan, "Dynamics of evanescently-coupled laser pairs with unequal pumping: Analysis using a three-variable reduction of the coupled rate equations," *IEEE J. Sel. Topics Quantum Electron.*, vol. 28, no. 1, pp. 1–9, Jan. 2022.

[45] E. J. Doedel *et al.*, *AUTO-07p: Continuation and Bifurcation Software for Ordinary Differential Equations*. Montreal, QC, Canada: Concordia Univ., 2008).

Mike Adams received the Ph.D. degree in laser theory from the University of Wales, Cardiff, U.K., in 1970. Since 1996, he has been a Professor with the University of Essex, Colchester, U.K. He is involved in optoelectronics research and development with 15 years of experience in industry (Plessey, BT) and 36 years in academia at the University of Cardiff; the University of Southampton, Southampton, U.K.; and the University of Essex. He has authored or coauthored widely in the optoelectronics field over many years, including a standard text on optical waveguide theory and two books on semiconductor lasers and optical fibers for use in telecommunications.

Nianqiang Li received the B.S. degree in communication engineering and the Ph.D. degree in optoelectronics from Southwest Jiaotong University, China, in 2008 and 2016, respectively. His thesis work concerned nonlinear dynamics of semiconductor lasers and its applications to secure communications and random number generation. From 2013 to 2014, he was a Visiting Scholar with the Georgia Institute of Technology (Georgia Tech), USA. From 2016 to 2018, he was with the School of Computer Science and Electronic Engineering, University of Essex, as a Post-Doctoral Researcher, focusing on a collaborative EPSRC funded project in U.K. From May 2018 to December 2018, he was with the School of Electrical Engineering and Computer Science, University of Ottawa, Canada, working on microwave photonics. He has been working with Soochow University as a Full Professor since January 2019. He has authored or coauthored more than 70 peer-reviewed journal articles. His current research mainly focuses on the area of the laser dynamics, chaos-based communication and random number generation, and microwave photonics. He is also an Associate Editor of IEEE ACCESS.

Yu Huang received the M.S. degree from Ludong University, China, in 2020. He is currently pursuing the Ph.D. degree with Soochow University, Suzhou, China. His research interests include the vertical cavity surface-emitting laser and nonlinear laser dynamics.

Pei Zhou (Member, IEEE) received the B.S. and Ph.D. degrees from the Nanjing University of Aeronautics and Astronautics (NUAA), Nanjing, China, in 2013 and 2019, respectively. From 2017 to 2018, he was a Visiting Scholar with the University of California at Los Angeles. He is currently working with the School of Optoelectronic Science and Engineering, Soochow University, Suzhou, China. His main research interests include microwave photonics, nonlinear laser dynamics, and optical chaos generation.

Ian Henning received the B.Sc. degree (Hons.) in applied physics and the Ph.D. degree from the University of Wales, Cardiff, U.K. He was with the Devices Division, British Telecom Research Laboratories, Martlesham Heath, specializing mainly in the theory and measurement of semiconductor lasers. In 2002, he was a Professor with the Department of Electronic Systems Engineering, University of Essex, Colchester, U.K.